

An eternal discrete time crystal beating the Heisenberg limit

Changyuan Lyu¹, Sayan Choudhury¹, Chenwei Lv¹, Yangqian Yan^{1,2,*} and Qi Zhou^{1,2,3†}

1. Department of Physics and Astronomy, Purdue University,
525 Northwestern Avenue, West Lafayette, IN 47907, USA

2. Center for Science of Information, Purdue University, West Lafayette, IN 47907, USA

3. Purdue Quantum Science and Engineering Institute, Purdue University,
1205 W State St, West Lafayette, West Lafayette, IN 47907, USA

(Dated: November 5, 2021)

A discrete time crystal (DTC) repeats itself with a rigid rhythm, mimicking a ticking clock set by the interplay between its internal structures and an external force [1–12]. DTCs promise profound applications in precision time-keeping and other quantum techniques. However, it has been facing a grand challenge of thermalization. The periodic driving supplying the power may ultimately bring DTCs to thermal equilibrium and destroy their coherence [13–15]. Here, we show that an all-to-all interaction delivers a DTC that evades thermalization and maintains quantum coherence and quantum synchronization regardless of spatial inhomogeneities in the driving field and the environment. Moreover, the sensitivity of this DTC scales with the total particle number to the power of three over two, realizing a quantum device of measuring the driving frequency or the interaction strength beyond the Heisenberg limit. Our work paves the way for designing novel non-equilibrium phases with long coherence time to advance quantum metrology.

A periodic driving may continuously pump energies into a DTC and eventually heat it up to the infinite temperature [13–15]. A number of schemes have been proposed to slow down the thermalization [4–6, 9], such as the many-body localization (MBL), the Floquet prethermalization and crypto-equilibrium. Compared with other schemes only retaining the coherence of DTCs within certain time scales, MBL is of particular interest. Disorder breaks an interacting system into localized l-bits to encode the memory of the initial state [16], and suppresses thermalization up to an arbitrarily long time scale. However, most studies have considered homogeneous drivings so far. In practice, the driving field may vary across a DTC and local perturbations may further amplify the spatial inhomogeneities, both preventing individual constituents of the DTC from synchronization and impeding applying DTCs in quantum technologies. Whereas MBL could stabilize a DTC against weak inhomogeneous perturbations to π -rotations [17], it is no longer powerful in the presence of strong inhomogeneities, as the exponentially decayed couplings between l-bits in MBL have readily weakened the synchronization between remote parts of a DTC in spite of the presence of interactions.

Fundamental questions naturally arise. (1) How to access a DTC that could maintain quantum coherence and quantum synchronization in the presence of arbitrarily strong inhomogeneous driving fields and local perturbations? (2) Furthermore, how to implement such a DTC to promote the precision of quantum metrology?

We consider N spin-1/2s described by a Hamiltonian,

$$H = H_{\text{int}} + \sum_n H_{\text{pul}} \delta(t - nT), \text{ where}$$

$$H_{\text{int}} = 2J \sum_{i < j} S_i^z S_j^z, \quad (1)$$

$$H_{\text{pul}} = \sum_i^N \theta_i S_i^y. \quad (2)$$

As shown in Fig. 1(a), J is the strength of an all-to-all interaction, which has been considered in the Lipkin-Meshkov-Glick model [18]. $\vec{S}_i = \frac{1}{2} \vec{\sigma}_i$ and $\vec{\sigma}_i$ are Pauli matrices (we have set $\hbar = 1$). Eq. (1) can be realized using spin-1/2s coupled to a cavity or a waveguide [19, 20], or particles with long-range interactions whose ranges are much larger than the system size. The equivalence between spin-1/2s and bosons also provides a natural realization of such interaction [21]. θ_i determines the angle rotated by the i th spin about the y -axis. The dependence of θ_i on i characterizes the spatial inhomogeneity of the rotations.

We prove that, when $JT = \pi$ is satisfied, any initial state returns to itself at $t = 2nT^-$ for any even $N \in 2\mathbb{Z}$ and any θ_i as an arbitrary function of i . t^- (t^+) denotes the time right before (after) a pulse is applied. This perfect revival delivers an eternal DTC that evades thermalization and is equipped with a strong synchronization even in the presence of a noisy environment. Previous works on normalized all-to-all interactions have considered the small J limit of Eq. (1) [21], not the optimal choice of JT discussed here.

Consider an initial state with m spin-ups and $N - m$ spin-downs, $|\Psi(0^-)\rangle = \prod_i |\eta\rangle_i$, where $\eta = \uparrow, \downarrow$. After the first pulse,

$$|\uparrow\rangle_i \rightarrow +\cos\left(\frac{\theta_i}{2}\right) |\uparrow\rangle_i + \sin\left(\frac{\theta_i}{2}\right) |\downarrow\rangle_i, \quad (3)$$

$$|\downarrow\rangle_i \rightarrow -\sin\left(\frac{\theta_i}{2}\right) |\uparrow\rangle_i + \cos\left(\frac{\theta_i}{2}\right) |\downarrow\rangle_i, \quad (4)$$

* yan281@purdue.edu

† zhou753@purdue.edu

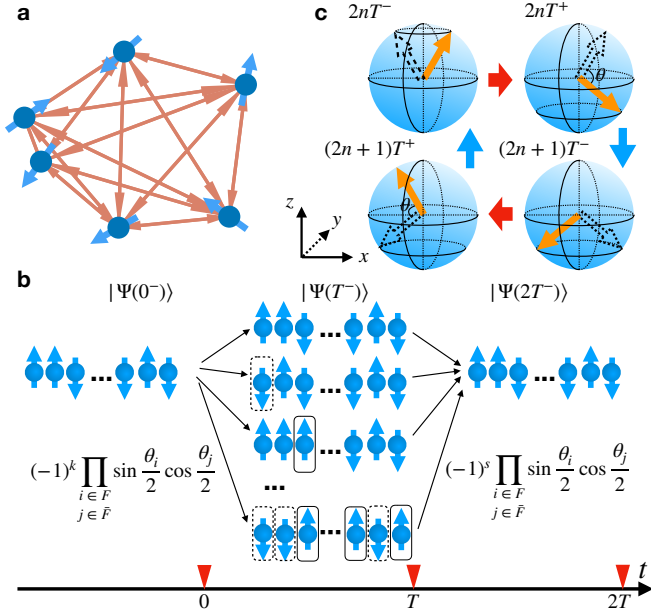


FIG. 1. A DTC induced by an all-to-all interaction. (a) Arrows represent an all-to-all interaction between spin-1/2s (blue spheres attached to arrows). (b) A perfect revival of an arbitrary initial state due to the constructive interference among all pathways. Dashed and solid boxes highlight the k spin-ups and s spin-downs flipped by the first pulse, which lead to the geometric phase, $(-1)^k$ and $(-1)^s$, respectively. (c) Rotations of the spin- L (yellow arrow) on the Bloch sphere. When $JT = \pi$, the non-linear term, JL_z^2 , leads to an effective π rotation about the z axis between $2nT^+$ and $(2n+1)T^-$ such that any initial state returns to the initial position after $2T$ for any θ . Triangles on the time axis represent H_{pul} .

$|\Psi(0^+)\rangle$ becomes a superposition of 2^N states, each of which is obtained from flipping s spin-ups and k spin-downs of $|\Psi(0^-)\rangle$, as shown in Fig. 1(b). Each state acquires a dynamical phase, $e^{-i\varphi_1}$, imposed by H_{int} from $t = 0^+$ to $t = T^-$. The second pulse flips the spins again, followed by H_{int} imposing another dynamical phase, $e^{-i\varphi_2}$, from $t = T^+$ to $t = 2T^-$, and

$$|\Psi(2T^-)\rangle = A |\Psi(0^-)\rangle + \dots, \quad (5)$$

where \dots represents states different from $|\Psi(0^-)\rangle$.

To return to $|\Psi(0^-)\rangle$, the s (k) spin-ups (spin-downs) flipped by the first pulse need to be flipped back to spin-ups (spin-downs) during the second pulse. 2^N such pathways allow the system to come back to $|\Psi(0^-)\rangle$. The contribution to A from each pathway is written as $(-1)^{k+s} \prod_{j \in \bar{F}} \cos^2(\frac{\theta_j}{2}) \prod_{i \in F} \sin^2(\frac{\theta_i}{2})$, where $(-1)^{k+s}$ comes from flipping $k + s$ spin-1/2s twice, equivalent to the geometric phase from rotating these spins about the y axis for 2π . F (\bar{F}) denotes the collection of flipped (unflipped) spins. As each of these 2^N states is an eigenstate of H_{int} , $\varphi_1 = (m - s + k)(m - s + k - N)\pi$, and $\varphi_2 = m(m - N)\pi$ when $JT = \pi$. m -independent terms have been dropped. The total dynamical

phase accumulated from 0^- to $2T^-$ is $e^{-i(\varphi_1 + \varphi_2)} = e^{i\pi\{2[m^2 + m(k-s-N) - ks] + N(s-k) + k^2 + s^2\}} = (-1)^{k+s}$. We have used $N \in 2\mathbb{Z}$, and $e^{iZ^2\pi} = e^{iZ\pi} = (-1)^Z$ for any integer Z . This dynamical phase factor cancels exactly the previously obtained geometric phase, and thus $A = \sum_F \prod_{j \in \bar{F}} \cos^2(\frac{\theta_j}{2}) \prod_{i \in F} \sin^2(\frac{\theta_i}{2})$. \sum_F denotes the sum over all 2^N choices of flipping the N spins in $|\Psi(0^-)\rangle$. Since F is an arbitrary choice from the N spins,

$$A = \prod_i (\sin^2(\frac{\theta_i}{2}) + \cos^2(\frac{\theta_i}{2})) = 1. \quad (6)$$

These discussions apply to any initial product state and any $t \in [2nT^-, 2(n+1)T^-]$. Thus, any initial state returns to itself at $t = 2nT^-$. Unlike traditional spin-echo schemes using tailored pulses to restore quantum coherence [22], we implement interactions, one source of the decoherence, to overcome the other, the inhomogeneities, so as to access a perfect dynamical localization, an analogue to the Anderson localization in the Hilbert space [23]. Therefore, this interaction induced spin-echo could be used in a broad class of systems to extend the coherence time.

For spatially uniform pulses, a simpler proof exists. H is rewritten as

$$H_{\text{hom}} = JL_z^2 + \theta L_y \sum_n \delta(t - nT), \quad (7)$$

where $\vec{L} = \sum_i \vec{S}_i$. Eq. (7) is equivalent to the kicked top model describing a periodically driven spin- L [24], where $L = \frac{N}{2}$. The propagator from $t = 2nT^-$ to $t = 2(n+1)T^-$ is written as

$$U_{JT}(2T) = e^{-iJTL_z^2} e^{-i\theta L_y} e^{-iJTL_z^2} e^{-i\theta L_y}. \quad (8)$$

As $e^{-i\pi L_z^2} = e^{-i\pi L_z}$ applies to any integer L (or even N), $U_\pi(2T) = e^{-2i\pi L_z} e^{i\pi L_z} (-i\theta L_y) e^{-i\pi L_z} e^{-i\theta L_y} = 1$. As shown by Fig. 1(c), any state on the Bloch sphere of a spin- L returns to the original place after $2T$. If $N \in 2\mathbb{Z} + 1$, $e^{-i\pi L_z^2}$ and $e^{-i\pi L_z}$ are no longer identical, and such DTC with a period of $2T$ does not exist. In contrast, if we consider spin-1 instead of spin-1/2 in Eq. (1), such even-odd effect is absent, as L is always an integer for both even and odd N .

$U_\pi(2T) = 1$ means that the quasi-energy spectrum of H_{eff} , where $U_{JT}(2T) = e^{-iH_{\text{eff}}}$, has 2^N degenerate eigenstates. Whereas this looks similar to the non-interacting case when $\theta_i = \pi$, a conceptual difference is that, the degeneracy here is stable against any perturbations in θ_i , unlike non-interacting systems, where any infinitesimal derivation from a homogeneous π -pulse lifts the degeneracy, breaks the integrability, and suppresses DTCs.

To highlight the stability against the spatial inhomogeneity, we compare the all-to-all interaction model to the power-law interaction model, $H' = H'_{\text{int}} + \sum_n H_{\text{pul}} \delta(t - nT)$, where

$$H'_{\text{int}} = 2J \sum_{i < j} \frac{S_i^z S_j^z}{|i - j|^\alpha}. \quad (9)$$

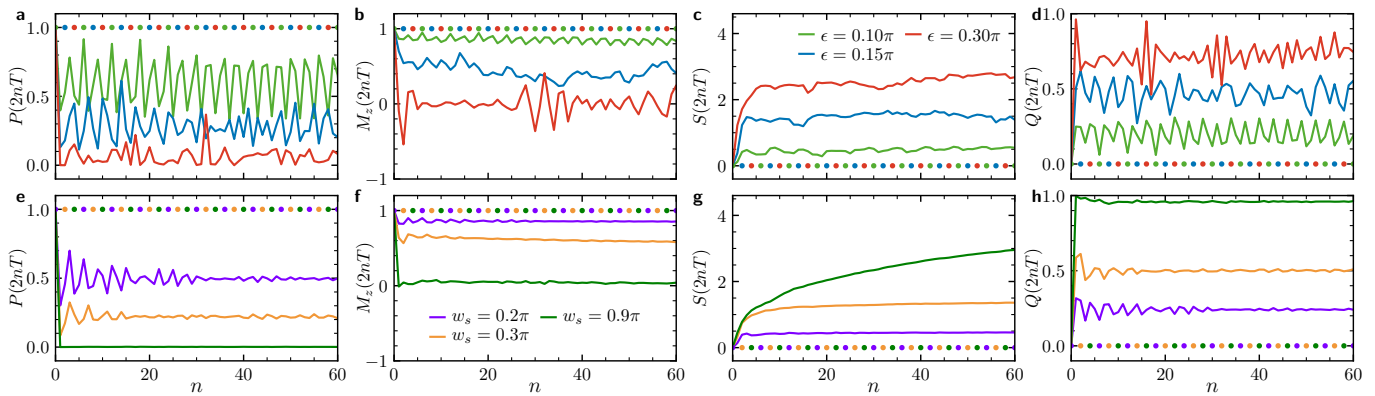


FIG. 2. Comparison between the all-to-all interaction and a power-law potential with $\alpha = 3$. Here $N = 14$. (a-d) Uniform rotations of spins, $w_s = 0$. The DTC with all-to-all interactions (dots) is unaffected by ϵ , the derivation of $\bar{\theta}$ from π . With the power-law potential (curves), increasing ϵ leads to the suppression of $P(2nT)$ and $M_z(2nT)$, and the growth of $S(2nT)$ and $Q(2nT)$. (e-h) Keeping $\bar{\theta} = \pi$ and increasing the spatial inhomogeneities w_s , the DTC with the power-law potential is suppressed. The DTC with all-to-all interactions remains stable.

Starting from $|\Psi(0^-)\rangle = \prod_i |\uparrow\rangle_i$, we compute some quantities for both interactions using exact diagonalization,

$$P(2nT^-) = |\langle \Psi(0^-) | \Psi(2nT^-) \rangle|^2, \quad (10)$$

$$M_z(2nT^-) = 2 \langle \Psi(2nT^-) | L_z | \Psi(2nT^-) \rangle / N, \quad (11)$$

$$E(2nT^-) = \langle \Psi(2nT^-) | H_{\text{int}} | \Psi(2nT^-) \rangle, \quad (12)$$

$$S(2nT^-) = -\text{Tr}(\rho_B \ln \rho_B). \quad (13)$$

$P(2nT^-)$ characterizes the quantum memory of the initial state, $M_z(2nT^-)$ denotes the z -component of the total spin, $E(2nT^-)$ (or $E'(2nT^-) = \langle \Psi(2nT^-) | H'_{\text{int}} | \Psi(2nT^-) \rangle$) captures the absorption of energy, and $S(2nT^-)$ is the bipartite entanglement entropy using the reduced density matrix of half of the system, ρ_B .

When $\theta_i = \bar{\theta}$ for any i , a finite J in Eq. (9) restores the quantum coherence, if $\epsilon = \bar{\theta} - \pi$ is small [6–8]. However, with increasing ϵ , both $P(2nT^-)$ and $M_z(2nT^-)$ get suppressed, as depicted in Fig. 2(a-d). Meanwhile, Q and S grow quickly, where we have used $Q = \frac{E(2nT^-) - E(0)}{E_\infty - E(0)}$ to characterize the absorption of the energy. $E_\infty = 2^{-N} \sum_j \langle j | H_{\text{int}} | j \rangle$ is the energy at the infinite temperature and $|j\rangle$ denotes the 2^N eigenstates of H_{int} . These results signify the thermalization at large ϵ . We further take into account the spatial inhomogeneity. As shown in Fig. 2(e-h), we choose a random θ_i from $[\bar{\theta} - w_s, \bar{\theta} + w_s]$ with a constant probability. When w_s is finite, the thermalization becomes even faster and Q approaches 1, indicating that the system thermalizes to the infinite temperature. Adding onsite disorder to introduce MBL does not change qualitative results (Supplementary Material). In contrast, $P(2nT^-)$ and $M_z(2nT^-)$ of the all-to-all interaction are unaffected by w_s and remain unity, and both $Q(2nT^-)$ and $S(2nT^-)$ remain zero, directly reflecting the robustness of this eternal DTC against arbitrarily strong spatial inhomogeneities and representing the most synchronized DTC.

We now discuss applications of this DTC. As aforementioned, the perfect revival at $t = 2nT^-$ comes from the same dynamical phase of all 2^N pathways of returning to $|\Psi(0)\rangle$ when $JT = \pi$. Once $JT \neq \pi$, these dynamical phases are no longer the same. In particular, the larger N is, the more rapidly the dynamical phase varies with changing the pathways. In the large N limit, this DTC becomes supersensitive to the value of JT and serves as a high precision device to measure either J or T .

Since it is time-consuming to solve more than 14 lattice sites using exact diagonalization when inhomogeneities exist, we focus on homogeneous systems. It is expected that the lower bound of the results of an inhomogeneous distribution, $\theta_i \in [\bar{\theta} - w_s, \bar{\theta} + w_s]$, could be estimated using homogeneous $\theta_i = \bar{\theta} \pm w_s$. As an example, we consider θ_i fixed at $\pi/4$. As shown in Fig. 3(a), $P(2nT^-)$ quickly vanishes if $|\delta| \gg \pi/N^{\frac{3}{2}}$, where $\delta = JT - \pi$. It is known that the Heisenberg limit, $1/N$, sets the bound of the precision in linear metrology, whereas non-linearity allows going beyond this limit [25]. The DTC discussed here represents a new category of nonlinear quantum metrology using periodic drivings.

We evaluate some observables to quantitatively characterize the sensitivity. $P(2T)$, the returning probability to $|\Psi(0^-)\rangle$ after two periods, captures short time dynamics. Fig. 3(c) shows that the dependence of $P(2T)$ on JT has a narrow peak centered at π , whose width is of the order of $1/N^{\frac{3}{2}}$. Such scaling can be obtained analytically (Supplementary Materials), and is verified numerically, as shown in the inset of Fig. 3(c). Another quantity is the power spectrum, $\hat{P}(f) = \frac{1}{M} \sum_{n=0}^{M-1} e^{i2\pi nTf} P(nT)$. We are particularly interested in $\hat{P}(f = \frac{1}{2T})$ characterizing the response of the DTC at half of the frequency of the periodic driving. The dependence of $\hat{P}(f)$ on JT also has a peak around π . We define the full width at half maximum as Δ_{JT} , and find both numerically and analytically that Δ_{JT} is proportional to $1/N^{\frac{3}{2}}$ (Supplementary

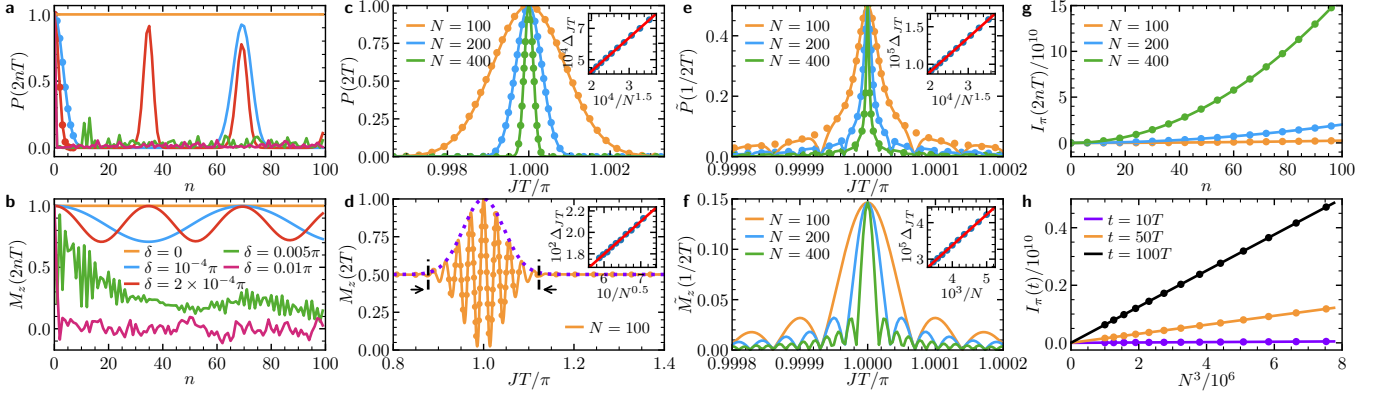


FIG. 3. Sensitivity to JT . Curves (dots) are numerical (analytical) results. (a,b) $P(2nT)$ and $M_z(2nT)$ as functions of n at various JT . When $|JT - \pi| \gg \pi/N^{3/2}$, both quantities quickly decrease down to zero. $N = 200$ has been used in the calculation. (c,d) $P(2T)$ and $M_z(2T)$ at a fixed time $t = 2T$ as a function of JT . For a fixed N , both $P(2T)$ and $M_z(2T)$ have narrow peaks centered at $JT = \pi$. Whereas $M_z(2T)$ has an additional fast oscillation, the dashed curve highlights the analytical result of its profile, whose width is denoted by black arrows. Insets show the scalings of the widths of the peaks with N . (e,f) The power spectra, $\tilde{P}(1/2T)$ and $\tilde{M}_z(1/2T)$, which contain information of both short and long-time dynamics, are also featured by narrow peaks around $JT = \pi$. $M = 200$ is used in numerics. Insets show the scaling of the widths of the peaks with N . (g) The quantum Fisher information $I_\pi(2nT)$ as a function of n . (h) $I_\pi(2nT)$ is proportional to N^3 . $\theta_i = \pi/4$ is used in all panels.

Material).

To gain insights into the scalings, we consider the quantum Fisher information,

$$I_{JT}(2nT) = \lim_{\epsilon \rightarrow 0} 4 \frac{1 - F_\epsilon}{\epsilon^2}, \quad (14)$$

$$F_\epsilon = |\langle \Psi(0^-) | U_{JT}(2nT) U_{JT+\epsilon}(-2nT) | \Psi(0^-) \rangle|^2, \quad (15)$$

where F_ϵ is the Loschmidt echo. The squared root of the quantum Fisher information limits the precision of a phase measurement [26]. The uncertainty of JT is bounded by $\sqrt{I_{JT}(2nT)}$, i.e., $\Delta_{JT} \geq 1/\sqrt{I_{JT}(2nT)}$. We have found analytically that (Supplementary Materials),

$$I_\pi(2nT) = \frac{n^2}{4} [\sin^2(2\bar{\theta})N^3 + 2\sin^4(\bar{\theta})N^2]. \quad (16)$$

When $\bar{\theta} \neq 0, \pm\pi/2, \pi$, $I_\pi(2nT) \sim n^2N^3$, provided that $\sin^2(2\bar{\theta})N^3 \gg 2\sin^4(\bar{\theta})N^2$. Thus, $I_\pi(2nT)$ scales with n^2N^3 in the large N limit, as shown in Fig. 3(g,h). Correspondingly, $\Delta_{JT} \geq 1/\sqrt{I_\pi(2nT)} \sim n^{-1}N^{-3/2}$. This is precisely what we have obtained in Fig. 3(c,e).

DTCs previously discussed in the literature are stable within a finite range of both the interaction strength and a uniform derivation of θ_i from π . In contrast, the all-to-all interaction induced DTC is stable against any spatial fluctuations in θ_i and meanwhile supersensitive to JT . In practice, it is much easier to control J and T other than the N local parameters θ_i in a noisy environment, where θ_i s may not have any correlations at different locations. Moreover, our DTC could be used to measure JT with high precision beyond the Heisenberg limit. It mimics a supersensitive clock. If the frequency of the external field, $\omega_d = 1/T$, is fixed, J , which corresponds to some

internal parameter of a clock, for instance, the length of a pendulum clock, needs to be tuned with a precision of $1/N^{3/2}$ to deliver rigid ticks at $t = 2nT$. Otherwise, this DTC stalls to avoid errors in the time-keeping. Our results thus lead to a new type of precision measurement of J . From $JT = \pi$, the precision of J can be estimated as $\Delta_J/J \approx \Delta_d/\omega_d + N^{-3/2}$, where Δ_d/ω_d characterizes the precision of the driving frequency. When $N^{-3/2} \gg \Delta_d/\omega_d$, Δ_J/J scalings with $N^{-3/2}$. When $N \rightarrow (\Delta_d/\omega_d)^{-2/3}$, the uncertainty of J eventually approaches the precision limit of Δ_d/ω_d . Whereas the precision of Δ_d/ω_d is up to 10^{-19} in the THz regime [27], typical experiments on ultracold atoms, ion traps and NV centers have interaction strengths $\sim 10^2 - 10^5$ Hz. In such regime, the precision of Δ_d/ω_d could be 10^{-6} and above. Our results thus provide a new application of precision time-keeping in many-body physics.

Alternatively, if J is fixed, the DTC discussed here could gauge the frequency, as only a driving field, whose T deviates from π/J within $1/N^{3/2}$, could induce its long-lasting dynamics. Different from atomic clocks using a transition with a narrow line width, the selection of the driving frequency here entirely comes from the many-body effect we previously discussed. In particular, the rotated angle, $\bar{\theta}$, can be arbitrary such that the DTC could function in a non-ideal environment, unlike previous works requiring a precise control of pulses in non-linear metrology without periodic driving [28–30]. Though $1/J$ may not be as precise as transition frequencies in atomic clocks, the many-body effect induced $1/N^{3/2}$ scaling could make this DTC a useful gauge of the frequency or time.

We have also studied the scalings of other quantities.

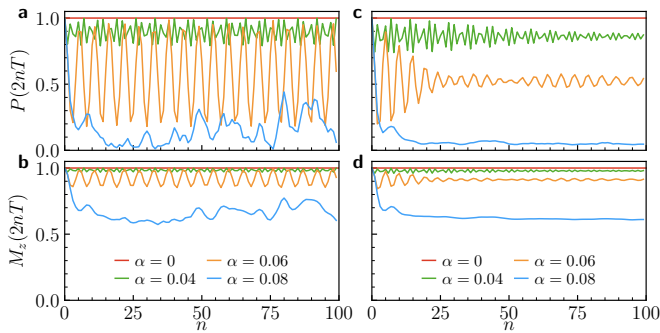


FIG. 4. Power-law potentials for $N = 14$. (a,b) Uniform rotations with $\bar{\theta} = 0.95\pi$. $\alpha = 0$ corresponds to the all-to-all interaction. With decreasing α , the results of the power-law potentials approach those of the all-to-all interaction. All parameters are the same in (a) and (b). (c,d) Inhomogeneous rotations with $\bar{\theta} = \pi$ and $w_s = 0.1\pi$.

We have found that $M_z(2T^-)$ and $\tilde{M}(\frac{1}{2T})$ scale with $1/N^{\frac{1}{2}}$ and $1/N$, respectively, as shown by Fig. 3(b,d,f). Similar scalings are obtained for other uniform rotations. For instance, when $\theta_i = \pi/2$, Δ_{JT} of either $\tilde{P}(\frac{1}{2T})$ or $\tilde{M}_z(\frac{1}{2T})$ scales with $1/N$ (Supplementary Materials).

Whereas we have been focusing on the all-to-all interaction, similar conclusions apply to a generic long-range interaction, provided that its range is much larger than the size of the system. For instance, with decreasing α , the range of the a power-law potential in Eq. (9) increases. When $\alpha = 0$, it is equivalent to the all-to-all interaction. Fig. 4 shows the results for $N = 14$. With decreasing α down to zero, $P(2nT)$ and $M_z(2nT)$ increase and eventually approach the result of the all-to-all interaction. A small $\alpha = 0.04$ readily provides us with a good approximation of the all-to-all interaction in such a finite system.

Both interactions and external drivings are crucial for DTCs. We hope that our work will stimulate more studies of their interplays to access novel non-equilibrium quantum states with long coherent time.

We acknowledge C.-L. Hung for helpful discussions on the precision of measuring frequencies. This work is supported by DOE DE-SC0019202, W. M. Keck Foundation, and the Center for Science of Information (CSoI), an NSF Science and Technology Center, under grant agreement CCF-0939370. C. Lv acknowledges support from Purdue Research Foundation.

-
- [1] Wilczek, F. Quantum time crystals. *Phys. Rev. Lett.* **109**, 160401 (2012).
- [2] Li, T. *et al.* Space-time crystals of trapped ions. *Phys. Rev. Lett.* **109**, 163001 (2012).
- [3] Watanabe, H. & Oshikawa, M. Absence of quantum time crystals. *Phys. Rev. Lett.* **114**, 251603 (2015).
- [4] Khemani, V., Lazarides, A., Moessner, R. & Sondhi, S. L. Phase structure of driven quantum systems. *Phys. Rev. Lett.* **116**, 250401 (2016).
- [5] Else, D. V., Bauer, B. & Nayak, C. Floquet time crystals. *Phys. Rev. Lett.* **117**, 090402 (2016).
- [6] Yao, N. Y., Potter, A. C., Potirniche, I.-D. & Vishwanath, A. Discrete time crystals: Rigidity, criticality, and realizations. *Phys. Rev. Lett.* **118**, 030401 (2017).
- [7] Choi, S. *et al.* Observation of discrete time-crystalline order in a disordered dipolar many-body system. *Nature* **543**, 221–225 (2017).
- [8] Zhang, J. *et al.* Observation of a discrete time crystal. *Nature* **543**, 217–220 (2017).
- [9] Abanin, D., Roeck, W. D., Ho, W. W. & Huse, F. A rigorous theory of many-body prethermalization for periodically driven and closed quantum systems. *Commun. Math. Phys.* **354**, 809–827 (2017).
- [10] Pal, S., Nishad, N., Mahesh, T. S. & Sreejith, G. J. Temporal order in periodically driven spins in star-shaped clusters. *Phys. Rev. Lett.* **120**, 180602 (2018).
- [11] Rovny, J., Blum, R. L. & Barrett, S. E. Observation of discrete-time-crystal signatures in an ordered dipolar many-body system. *Phys. Rev. Lett.* **120**, 180603 (2018).
- [12] Huang, B., Wu, Y.-H. & Liu, W. V. Clean floquet time crystals: Models and realizations in cold atoms. *Phys. Rev. Lett.* **120**, 110603 (2018).
- [13] D’Alessio, L. & Rigol, M. Long-time behavior of isolated periodically driven interacting lattice systems. *Phys. Rev. X* **4**, 041048 (2014).
- [14] Ponte, P., Chandran, A., Papić, Z. & Abanin, D. A. Periodically driven ergodic and many-body localized quantum systems. *Ann. Phys. (N. Y.)* **353**, 196–204 (2015).
- [15] Lazarides, A., Das, A. & Moessner, R. Equilibrium states of generic quantum systems subject to periodic driving. *Phys. Rev. E* **90**, 012110 (2014).
- [16] Pal, A. & Huse, D. A. Many-body localization phase transition. *Phys. Rev. B* **82**, 174411 (2010).
- [17] von Keyserlingk, C. W., Khemani, V. & Sondhi, S. L. Absolute stability and spatiotemporal long-range order in floquet systems. *Phys. Rev. B* **94**, 085112 (2016).
- [18] Lipkin, H., Meshkov, N. & Glick, A. Validity of many-body approximation methods for a solvable model. *Nucl. Phys.* **62**, 188–198 (1965).
- [19] Hung, C.-L., González-Tudela, A., Cirac, J. I. & Kimble, H. J. Quantum spin dynamics with pairwise-tunable, long-range interactions. *Proc. Natl. Acad. Sci. U.S.A.* **113**, E4946–E4955 (2016).
- [20] Ritsch, H., Domokos, P., Brennecke, F. & Esslinger, T. Cold atoms in cavity-generated dynamical optical potentials. *Rev. Mod. Phys.* **85**, 553–601 (2013).
- [21] Russomanno, A., Iemini, F., Dalmonte, M. & Fazio, R. Floquet time crystal in the lipkin-meshkov-glick model. *Phys. Rev. B* **95**, 214307 (2017).
- [22] Yan, B. *et al.* Observation of dipolar spin-exchange interactions with lattice-confined polar molecules. *Nature* **501**, 521–525 (2013).
- [23] D’Alessio, L. & Polkovnikov, A. Many-body energy localization transition in periodically driven systems. *Ann.*

- Phys. (N. Y.)* **333**, 19–33 (2013).
- [24] Haake, F., Kuś, M. & Scharf, R. Classical and quantum chaos for a kicked top. *Z. Phys. B* **65**, 381–395 (1987).
- [25] Braun, D. *et al.* Quantum-enhanced measurements without entanglement. *Rev. Mod. Phys.* **90**, 035006 (2018).
- [26] Helstrom, C. W. Quantum detection and estimation theory. *J. Stat. Phys.* **1**, 231–252 (1969).
- [27] Marti, G. E. *et al.* Imaging optical frequencies with 100 μHz precision and 1.1 μm resolution. *Phys. Rev. Lett.* **120**, 103201 (2018).
- [28] Rey, A. M., Jiang, L. & Lukin, M. D. Quantum-limited measurements of atomic scattering properties. *Phys. Rev. A* **76**, 053617 (2007).
- [29] Choi, S. & Sundaram, B. Bose-einstein condensate as a nonlinear ramsey interferometer operating beyond the heisenberg limit. *Phys. Rev. A* **77**, 053613 (2008).
- [30] Napolitano, M. *et al.* Interaction-based quantum metrology showing scaling beyond the heisenberg limit. *Nature* **471**, 486–489 (2011).

Supplemental Material of “An eternal discrete time crystal beating the Heisenberg limit”

I. ONSITE DISORDER

The onsite disorder is often considered in DTC to introduce many-body localization. Since the coupling between l-bits decays exponentially with increasing their distance, this could slow down the thermalization, provided that θ_i is spatially uniform. However, this mechanism of suppressing the thermalization automatically weakens the synchronization between different spatial parts of the system. Thus, when θ_i has strong spatial inhomogeneities, the onsite disorder cannot stabilize the DTC. Consider the Hamiltonian,

$$H = 2J \sum_{i < j} \frac{S_i^z S_j^z}{|i-j|^\alpha} + \sum_n \delta(t - nT) \sum_{i=1}^N \theta_i S_i^y + 2 \sum_{i=1}^N \Delta_i S_i^z, \quad (\text{S1})$$

where θ_i has a uniform distribution in $[\bar{\theta} - w_s, \bar{\theta} + w_s]$, similar to the main text. The onsite disorder, Δ_i , has a uniform distribution in $[0, W]$. As shown in Fig. S1, for a given W , with increasing w_s , $P(2nT)$ and $L_z(2nT)$ are suppressed down to zero. Meanwhile, the entropy $S(2nT)$ and $Q(2nT)$ grow faster, signifying the thermalization of the DTC.

II. SCALINGS WITH PARTICLE NUMBERS

A. Scalings at $t = 2T$

We have analytically obtained how the dependence of $P(2T)$ ($M_z(2T)$) on JT scales with the particle number N ,

$$P'(\delta) \equiv P(2T; JT = \pi + \delta) = \left(1 + \frac{N^2 \delta^2 \sin^4 \theta}{4}\right)^{-1/2} e^{-\frac{1}{4N^2 \delta^2 \sin^4 \theta + 16} \sin^2(2\theta) \delta^2 N^3}, \quad (\text{S2})$$

$$M'_z(\delta) \equiv M_z(2T; JT = \pi + \delta) = \cos^2 \theta + \sin^2 \theta \cos(\cos \theta N \delta) e^{-\frac{N}{2} \delta^2 \sin^2 \theta}. \quad (\text{S3})$$

When $\theta = \pi/2$, $\sin(2\theta) = 0$. The exponential function in Eq. (S2) becomes identity, and $P'(\delta) = \left(1 + \frac{N^2 \delta^2 \sin^4 \theta}{4}\right)^{-1/2}$. Thus, the peak width shown in Fig. S2 scales with $1/N$. The same scaling applies to θ near 0 and π . In contrast, when θ is away from 0, $\pi/2$ and π , the exponential function becomes dominant, and $P(2T)$ decays faster, as shown in Fig. 3(c) of the main text. In particular, the peak width of $P(2T)$ in Fig. 3(e) scales with $1/N^{3/2}$.

In Eq. (S3), the $N\delta$ term in the cosine function leads to a fast oscillation, and the $N\delta^2$ term in the exponential function leads to the $1/N^{1/2}$ scaling of the profile of $M_z(2T)$, regardless of θ , as shown in the insets of Fig. S2(d) of this supplementary material and Fig. 3(d) of the main text.

To derive Eq. (S2) and Eq. (S3), we consider an initial state, $|\Psi(0^-)\rangle = \prod_i |\uparrow\rangle_i = |\frac{N}{2}, \frac{N}{2}\rangle$, where $L_z |\frac{N}{2}, l\rangle = l |\frac{N}{2}, l\rangle$ and $\frac{N}{2} = L$ is the total angular momentum.

$$\begin{aligned} P'(\delta) &= |\langle \Psi(0^-) | e^{-i(\pi+\delta)L_z^2} e^{-i\theta L_y} e^{-i(\pi+\delta)L_z^2} e^{-i\theta L_y} | \Psi(0^-) \rangle|^2 \\ &= |e^{-i(\pi+\delta)(\frac{N}{2})^2} \langle \Psi(0^-) | e^{-i\theta L_y} e^{-i(\pi+\delta)L_z^2} e^{-i\theta L_y} | \Psi(0^-) \rangle|^2. \end{aligned} \quad (\text{S4})$$

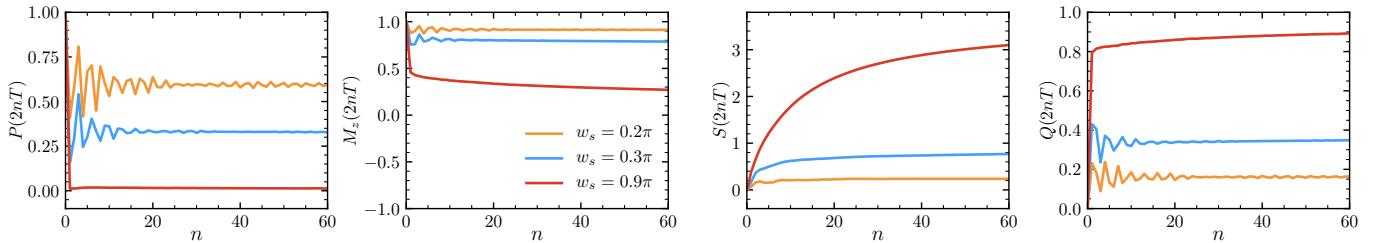


FIG. S1. Effects of inhomogeneous θ_i on MBL. θ_i is chosen from a uniform distribution $[-w_s + \bar{\theta}, \bar{\theta} + w_s]$. The onsite disorder is chosen from $[0, W]$, where $W = 40J$, $\alpha = 3$, $\bar{\theta} = \pi$, $N = 14$.

As discussed in the main text, $e^{-i\pi L_z^2} = e^{-i\pi L_z}$ is satisfied for any even particle number N . When δ is small, $e^{-i\delta L_z^2}$ can be written as $e^{-i\delta L_z^2} \approx \int_{-N\delta}^{N\delta} dk e^{ik^2/4\delta} \frac{1}{2\pi} \frac{\sqrt{\pi}}{\sqrt{i\delta}} e^{-ikL_z}$. We thus obtain

$$P'(\delta) \approx |e^{-i(\pi+\delta)(\frac{N}{2})^2} \int_{-N\delta}^{N\delta} dk e^{ik^2/4\delta} \frac{1}{2\pi} \frac{\sqrt{\pi}}{\sqrt{i\delta}} I(\theta, k)|^2, \quad (\text{S5})$$

$$I(\theta, k) = \langle \Psi(0^-) | e^{-i\theta L_y} e^{-i\pi L_z} e^{-ikL_z} e^{-i\theta L_y} | \Psi(0^-) \rangle. \quad (\text{S6})$$

Note that $e^{-i\theta L_y} | \Psi(0^-) \rangle = | \theta, 0 \rangle_c$, $e^{i\pi L_z} e^{i\theta L_y} | \Psi(0^-) \rangle = (-1)^{\frac{N}{2}} | \theta, 0 \rangle_c$, we obtain

$$I(\theta, k) = (-1)^{\frac{N}{2}} \langle \theta, 0 |_c e^{-ikL_z} | \theta, 0 \rangle_c = (-1)^{\frac{N}{2}} e^{ik\frac{N}{2}} \left(\frac{1}{1+\alpha} \right)^N (e^{-ik\alpha} + 1)^N, \quad (\text{S7})$$

where $\alpha \equiv \tan^2 \frac{\theta}{2}$ and

$$| \theta, \phi \rangle_c = \sum_{l=-N/2}^{N/2} \sqrt{\frac{N!}{(\frac{N}{2}+l)!(\frac{N}{2}-l)!}} (\cos \theta)^{\frac{N}{2}+l} (\sin \theta)^{\frac{N}{2}-l} e^{i\phi(\frac{N}{2}-l)} | l \rangle \quad (\text{S8})$$

is a coherent state pointing along θ, ϕ . In the large N limit,

$$I(\theta, k) \approx (-1)^{\frac{N}{2}} e^{-ik\frac{N}{2} + i\frac{N}{1+\alpha}k} e^{-\frac{N}{2} \frac{\alpha}{(1+\alpha)^2} k^2}, \quad (\text{S9})$$

which represents a narrow Gaussian centered at $k = 0$. Substituting $I(\theta, k)$ in Eq. (S5) by Eq. (S9), we obtain Eq. (S2).

As for $M'_z(\delta)$, using the time evolution operator $U(T) = e^{-iL_z^2 JT} e^{-iL_y \theta}$, we obtain the Heisenberg equations, which provide us with the nonlinear recursion relations as shown in [1],

$$\begin{aligned} L'_x &= U^{-1}(T) L_x U(T) = \frac{1}{2} (L_x \cos \theta + L_z \sin \theta + iL_y) e^{i2JT(L_z \cos \theta - L_x \sin \theta + \frac{1}{2})} + h.c. \\ L'_y &= U^{-1}(T) L_y U(T) = \frac{1}{2i} (L_x \cos \theta + L_z \sin \theta + iL_y) e^{i2JT(L_z \cos \theta - L_x \sin \theta + \frac{1}{2})} + h.c. \\ L'_z &= U^{-1}(T) L_z U(T) = L_z \cos \theta - L_x \sin \theta. \end{aligned} \quad (\text{S10})$$

Since $M_z(2T) = \frac{2}{N} \langle \Psi(0^-) | U^{-1}(T) U^{-1}(T) L_z U(T) U(T) | \Psi(0^-) \rangle$, we obtain,

$$\begin{aligned} M'_z(\delta) &= \frac{2}{N} \langle \Psi(0^-) | [(L_z \cos \theta - L_x \sin \theta) \cos \theta \\ &\quad - \left(\frac{1}{2} (L_x \cos \theta + L_z \sin \theta + iL_y) e^{i2JT(L_z \cos \theta - L_x \sin \theta + \frac{1}{2})} + h.c. \right) \sin \theta] | \Psi(0^-) \rangle \\ &= \cos^2 \theta - (-1)^{\frac{N}{2}} \sin \theta [\sin \theta \cos^N \frac{\Theta}{2} \cos(JT - N\Phi) + (\cos \theta + 1) \cos^N \frac{\Theta}{2} \tan \frac{\Theta}{2} \cos(\Phi + JT - N\Phi)] \\ &= \cos^2 \theta + (-1)^{\frac{N}{2}} \sin \theta \cos^N \left(\frac{\Theta}{2} \right) [\sin \theta \cos(\delta - N\Phi) + (\cos \theta + 1) \tan \frac{\Theta}{2} \cos(\Phi + \delta - N\Phi)] \\ &\approx \cos^2 \theta + \sin^2 \theta \cos(\cos \theta N\delta) e^{-\frac{N}{2} \delta^2 \sin^2 \theta} \end{aligned} \quad (\text{S11})$$

where $\Theta = \arccos(\cos^2 \theta + \cos(2\delta) \sin^2 \theta)$, $\Phi = \arctan\left(\frac{-\sin \theta \sin(2\delta)}{\cos \theta \sin \theta (-1 + \cos(2\delta))}\right)$. The expression which contains Θ and Φ is exact for any θ and δ 's. The final approximation comes from $\Theta^2 = 4 \sin^2 \theta \delta^2 + O(\delta^4)$, $\Phi = \pi/2 - \cos \theta \delta + O(\delta^3)$ and $\cos^N \frac{\Theta}{2} \approx e^{-N\delta^2 \sin^2 \theta/2}$ when δ is small and N is large. The overall profile as shown in Fig. 3(d) of the main text is thus given by $e^{-\frac{N}{2} \sin^2 \theta \delta^2} \sin^2 \theta + \cos^2 \theta$.

B. Scalings of $\tilde{P}(\frac{1}{2T})$

We have also obtained an analytical form for $\tilde{P}(f)$, the Fourier transform of $P(2nT)$. As shown in Fig. S3, starting from an initial state at the north pole, the state at $t = 2T^-$ covers a finite small region near the north pole, if $\delta = JT - \pi$ is small. The length scales of the longitude and latitude directions are proportional to δ and δ^2 , the

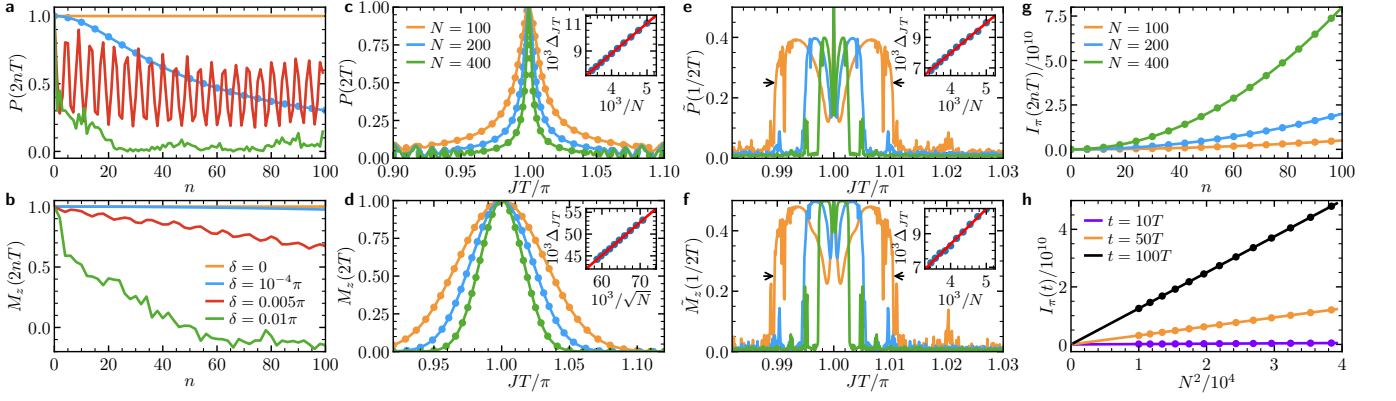


FIG. S2. Sensitivity of the DTC to JT when $\theta = \pi/2$. Dots are analytical results and curves are the numerical results. (a,b) $P(2nT)$ and $M_z(2nT)$ as functions of n for various JT . When $|JT - \pi| \gg \pi/N$ (here $N=200$), both quantities quickly decrease down to zero. (c,d) $P(2T)$ and $M_z(2T)$ at a fixed time $t = 2T$ as functions of JT . For a fixed N , both quantities are featured with narrow peaks centered at $JT = \pi$. Insets show the scalings of the widths Δ (full width at half maximum) of the peaks with N . (e,f) The power spectra $\tilde{P}(1/2T)$ and $\tilde{M}_z(1/2T)$ are also featured with narrow peaks around $JT = \pi$. Whereas they exhibit non-monotonic behaviors near $JT = \pi$, both quantities vanish when $|JT - \pi| \gg \pi/N$. Insets show the scalings of the widths of the peaks with N . (g) The quantum Fisher information $I_\pi(2nT)$ as a function of n . (h) $I_\pi(2nT)$ is proportional to N^2 . $\theta_i = \pi/2$ is used in all panels.

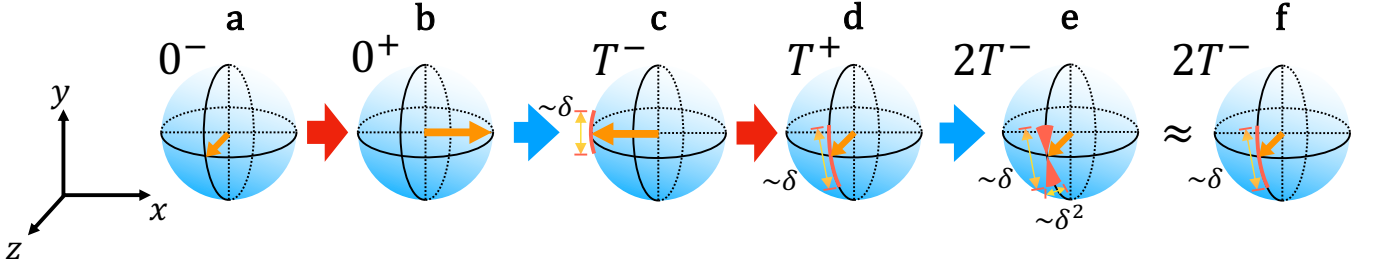


FIG. S3. The approximation used to derive $P(2nT)$. When $t = T^-$, the nonlinear operator $e^{-iJTL_z^2}$ creates a superposition of coherent states, which spans a length scale $\sim \delta$ in the latitude direction, as shown in (c). This length scale is transferred to the longitude direction around the north pole by the pulse at $t = T^+$, as shown in (d). Then the nonlinear operator creates a superposition of coherent states in the region highlighted by the red color at $t = 2T^-$. The length scales of this region in the longitude and latitude directions are δ and δ^2 respectively, as shown in (e). Replacing the second nonlinear operator $e^{-iJTL_z^2}$ by $e^{-i\pi L_z^2}$, as shown in (f), we have ignored the expansion of the wavefunction in the latitude direction that gives rise to a high order correction to $P(2nT)$ at small times.

latter of which can be ignored in the small δ limit. Thus, we make use of the following approximation to capture the dynamics in the small δ limit,

$$U(2T) = e^{-iJTL_z^2} e^{-i\theta L_y} e^{-iJTL_z^2} e^{-i\theta L_y} \approx e^{-i\pi L_z^2} e^{-i\theta L_y} e^{-iJTL_z^2} e^{-i\theta L_y}. \quad (\text{S12})$$

$P(2nT)$ is written as

$$P(2nT) = |\langle \Psi(0^-) | (e^{-i\pi L_z^2} e^{-i\theta L_y} e^{-i(\pi+\delta)L_z^2} e^{-i\theta L_y})^n | \Psi(0^-) \rangle|^2. \quad (\text{S13})$$

Using the identities, $e^{-i\pi L_z^2} = e^{-i\pi L_z}$ and $e^{-i\pi L_z} e^{-i\theta L_y} e^{-i\pi L_z} = e^{i\theta L_y}$, the equation above can be written as

$$P(2nT) = |\langle \Psi(0^-) | (e^{i\theta L_y} e^{-i\delta L_z^2} e^{-i\theta L_y})^n | \Psi(0^-) \rangle|^2 = |\langle \Psi(0^-) | e^{i\theta L_y} e^{-in\delta L_z^2} e^{-i\theta L_y} | \Psi(0^-) \rangle|^2. \quad (\text{S14})$$

Applying Eq. (S2), we obtain

$$P(2nT) = e^{-\frac{n^2 \sin^2(2\theta) \delta^2 N^3}{4N^2 n^2 \delta^2 \sin^4 \theta + 16}} \left(1 + \frac{n^2 N^2 \delta^2 \sin^4 \theta}{4}\right)^{-1/2}. \quad (\text{S15})$$

Eq. (S15) recovers Eq. (S2) when $n = 1$. As shown in Fig. S2(a), this expression well captures the initial decay of $P(2nT)$. However, it cannot describe the revival of $P(2nT)$ in later times for certain JT due to the made approximation in Eq. (S12).

The power spectrum is therefore written as

$$\tilde{P}(1/2T) = \frac{1}{M} \sum_{n=0}^{M-1} P(nT) e^{i \frac{2\pi}{2T} nT} = \frac{1}{M} \sum_{n=0}^{M-1} P(nT) (-1)^n \approx \frac{1}{M} \sum_{n=0}^{M/2-1} P(2nT), \quad (\text{S16})$$

where M is the cutoff required in numerics. In the last step, we have used the fact that, for small n , $|\psi(2nT + T)\rangle$ is located at a place on the Bloch sphere away from the north pole, provided that θ is not small, and thus, $P(2nT + T) = |\langle \Psi(0^-) | \psi(2nT + T) \rangle|^2 \approx 0$.

When $nN\delta \ll 1$ and $\theta \neq 0, \pi/2, \pi$, Eq. (S15) becomes $P(2nT) = e^{-\frac{n^2 \sin^2(2\theta) \delta^2 N^3}{16}}$, and Eq. (S16) is rewritten as

$$\tilde{P}(1/2T) \approx \frac{2\sqrt{\pi} \text{Erf}(\frac{1}{8} \delta M N^{3/2} \sin(2\theta))}{\sin(2\theta) \delta M N^{3/2}}, \quad (\text{S17})$$

In the limit $M \rightarrow \infty$, $\tilde{P}(1/2T) \rightarrow \frac{1}{2\sqrt{\pi}} e^{-\frac{1}{64} \delta^2 N^3 M^2}$. To compare with numerical result, we choose $\theta = \pi/4$ and $M = 200$. Eq. (S17) becomes

$$\tilde{P}(1/2T) \approx \frac{2\sqrt{\pi} \text{Erf}(25\delta N^{3/2})}{200\delta N^{3/2}}, \quad (\text{S18})$$

which shows the $1/N^{3/2}$ scaling. Erf is the error function. The comparison between this analytical result and the numerical one is shown in Fig. 3(e) of the main text.

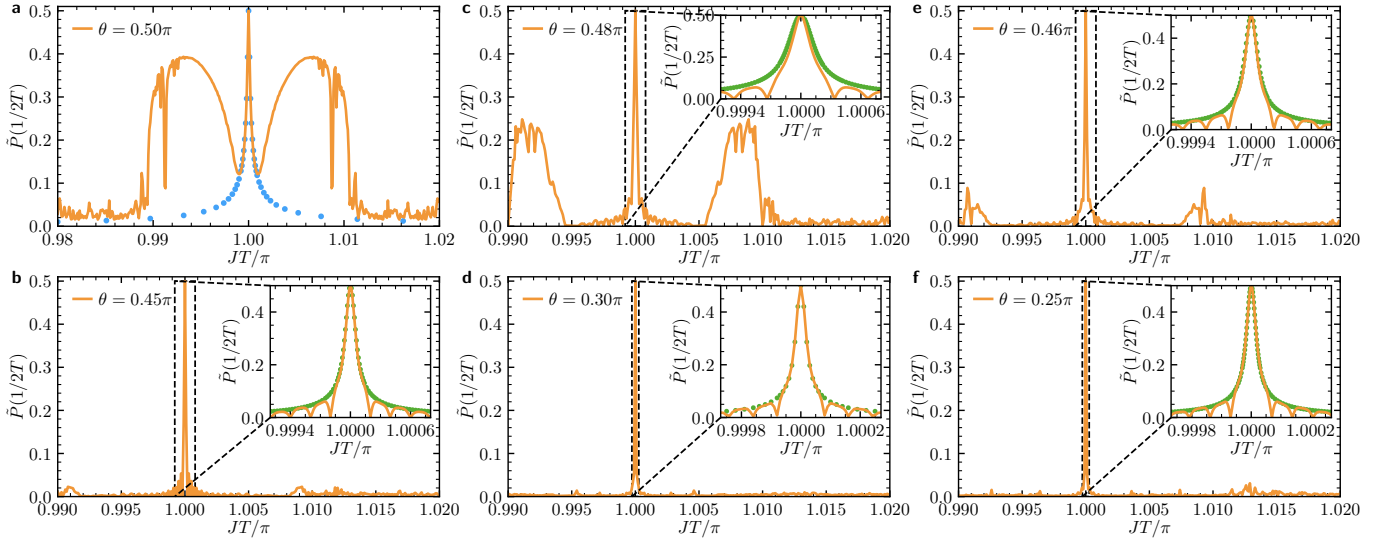


FIG. S4. The power spectra $\tilde{P}(1/2T)$ for different pulses for $N = 100$, $M = 200$. (a) It is identical to the curve for $N = 100$ in Fig. S2(e). The central sharp peak at $JT = \pi$ for $\pi/2$ pulse is well approximated by the analytical result (blue dots) shown in Eq. (S19). (b-f) When θ decreases, the two broader peaks gradually vanish. When the exponential term in Eq. (S15) dominates, the central peak is described by Eq. (S17) (green dots). Enlarging (f) around $JT = \pi$ gives rise to Fig. 3(e) of the main text.

When $\theta = \pi/2$, the exponential term in Eq. (S15) becomes identity. We obtain

$$\tilde{P}(1/2T) \approx \frac{\text{arcsinh}(\delta M N/4)}{\delta M N/2}. \quad (\text{S19})$$

As mentioned in Fig. S2, when $\theta = \pi/2$, the dependence of $\tilde{P}(1/2T)$ on JT is not monotonic. With increasing δ , $\tilde{P}(1/2T)$ first quickly decreases and then increases before it eventually vanishes when $\delta > \pi/N$. Eq. (S19) captures the narrow peak, whose width is much smaller than π/N , near $\delta = 0$. The broader peak scales with $1/N$ as shown in Fig. S2(f) of the main text. When θ deviates from $\pi/2$, the broader peak gets suppressed as shown in Fig. S4. When $\theta = \pi/4$, only the central narrow peak is visible, whose width scales with $1/N^{3/2}$, as discussed before.

$\tilde{M}_z(2nT)$ and $\tilde{M}_z(1/2T)$ do not have simple analytical forms. We have numerically evaluated them and the scaling of $\tilde{M}_z(1/2T)$ with N is shown in Fig. S2(b, e).

III. QUANTUM FISHER INFORMATION

When $JT = \pi$, the quantum Fisher information is written as

$$I_\pi(2nT) = \lim_{\epsilon \rightarrow 0} 4 \frac{1 - F_\epsilon}{\epsilon^2}, \quad (\text{S20})$$

$$F_\epsilon = |\langle \Psi(0^-) | U_\pi(-2nT) U_{\pi+\epsilon}(2nT) | \Psi(0^-) \rangle|^2. \quad (\text{S21})$$

As $U_\pi(2nT) | \Psi(0^-) \rangle = | \Psi(0^-) \rangle$ or equivalently, $\langle \Psi(0^-) | U_\pi(-2nT) = \langle \Psi(0^-) |$, the Loschmidt echo is identical to the quantum memory of the initial state, $F_\epsilon = |\langle \Psi(0^-) | U_{\pi+\epsilon}(2nT) | \Psi(0^-) \rangle|^2$. Using Eq. (S15) and replacing ϵ by δ , we obtain

$$I_\pi(2nT) = \lim_{\delta \rightarrow 0} 4 \frac{1 - P(2nT)}{\delta^2} = \frac{n^2 N^3 \sin^2(2\theta)}{4} + \frac{n^2 N^2 \sin^4 \theta}{2}. \quad (\text{S22})$$

[1] F. Haake, M. Kuś, and R. Scharf, Classical and quantum chaos for a kicked top, *Z. Phys. B* **65**, 381 (1987).